

# Diagnosing Direct-Drive, Shock-Heated, and Compressed Plastic Planar Foils with Noncollective Spectrally Resolved X-Ray Scattering

## Introduction

The achievement of energy gain with a direct-drive inertial confinement fusion (ICF) ignition target requires an accurate prediction of the shock-heated and compressed conditions in the main fuel layer.<sup>1</sup> A direct-drive ICF target for hot-spot ignition consists of a spherical cryogenic main fuel layer of deuterium and tritium surrounded by a thin plastic layer.<sup>1–3</sup> Intense laser beams uniformly irradiate the target and launch a shock wave through the main fuel layer. The pressure in the shock-heated shell determines the implosion performance of the target. The laser pulse for a direct-drive implosion consists of a low-intensity foot and high-intensity main drive. The low-intensity foot launches a relatively weak shock to isentropically compress the target, and the main drive sends a compression wave that implodes the target to form a central hot spot with sufficient fuel areal density and temperature to ignite the target. The entropy of the main fuel layer or shell adiabat  $\alpha$  is defined as the ratio of the pressure in the main fuel layer to the Fermi-degenerate pressure. It is a critical parameter in ICF because it is related to the minimum laser drive energy needed for ignition and the growth rate of the Rayleigh–Taylor (RT) hydrodynamic instability.<sup>4,5</sup> The RT instability distorts the uniformity of the implosion, reduces the target compression, and could prevent hot-spot formation.<sup>6</sup> Therefore, the successful target design for a stable, high-performance ICF implosion creates an adiabat in the shell that strikes a balance between the target stability and the laser-energy requirements.

The shock-heated shell in direct-drive ICF is predicted to have plasma conditions in the warm dense matter (WDM) regime.<sup>7</sup> The coupling parameter<sup>8</sup>  $\Gamma$  and ratio of Fermi temperature to electron temperature  $\Theta$  characterize plasmas in  $T_e$ – $n_e$  space. The electron–electron coupling parameter  $\Gamma_{ee}$  is the ratio of Coulomb potential between free electrons to the average kinetic energy of the free electrons:

$$\Gamma_{ee} = \frac{e^2}{dk_B T_e}, \quad (1)$$

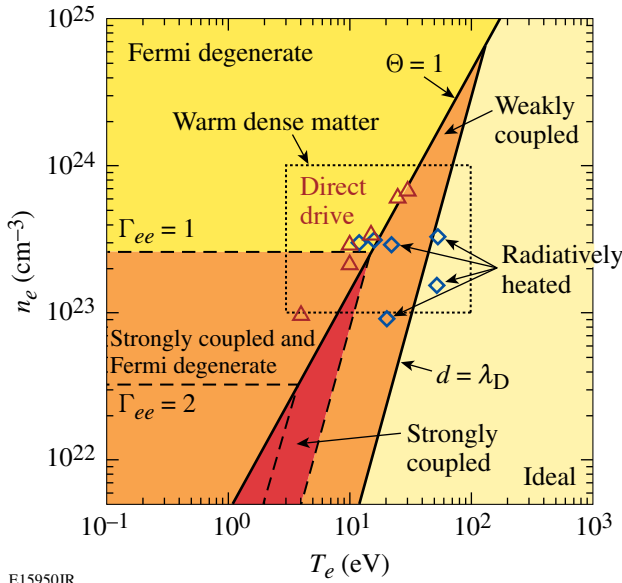
where  $d = (3/4\pi n_e)^{1/3}$  is the average interparticle spacing. When a plasma is strongly coupled ( $\Gamma_{ee} \gg 1$ ), the Coulomb interac-

tions between particles determine the physical properties of the plasma. When  $\Gamma_{ee} \ll 1$ , plasma behaves as an ideal gas and the interparticle coupling is insignificant. Similar considerations can be made with regards to the electron–ion and ion–ion coupling parameters.<sup>8</sup> In an ICF implosion, the shock-heated shell becomes a partially or fully degenerate plasma. The degree of degeneracy is described as

$$\Theta = T_F/T_e, \quad (2)$$

where  $T_F$  is the Fermi temperature [ $T_F = \hbar^2(3\pi^2 n_e)^{2/3}/2m_e k_B$ ,  $k_B$  is the Boltzmann constant]. In degenerate plasmas, the electron energy depends only on  $n_e$ , and the coupling constant is defined as the ratio between the potential and Fermi energy ( $\Gamma_{ee} = e^2/dE_F$ ). Figure 111.53 shows  $T_e$ – $n_e$  space characterized by the electron coupling parameter,  $\Gamma_{ee}$ ; the ratio of the  $T_e$  and  $T_F$ ,  $\Theta(T_F/T_e)$ ; the average interparticle spacing  $d = (3/4\pi n_e)^{1/3}$ ; and the Debye length  $\lambda_D$ . The plane is divided by the lines  $\Theta = 1$ ,  $\Gamma_{ee} = 1$ , and  $d = \lambda_D$  into regions where Fermi-degenerate, strongly coupled, Fermi-degenerate and strongly coupled, weakly coupled, and ideal plasmas exist. As shown in Fig. 111.53, the predicted conditions for the direct-drive experiments (see triangle symbols) lie in the WDM regime on the boundary between Fermi-degenerate, strongly coupled, and weakly coupled plasmas.

Diagnosing WDM is challenging because the temperature of the plasma is too low ( $\sim 10$  eV) for it to emit x rays and dense plasmas above the critical density cannot be probed with optical lasers for Thomson-scattering measurements.<sup>9</sup> Two viable techniques exist to diagnose these plasmas: spectrally resolved x-ray scattering<sup>10</sup> and time-resolved x-ray absorption spectroscopy.<sup>11</sup> X-ray absorption spectroscopy measurements provide time-resolved local measurements of the plasma conditions in the shock-heated foil; they require, however, a buried mid-Z tracer layer such as Al. The Al  $1s$ – $2p$  absorption spectroscopy was used to diagnose similar plasma conditions in a direct-drive, shock-heated CH planar foil by using a point-source Sm backlighter.<sup>12</sup> The spectrally resolved x-ray scattering does not require a tracer layer; it requires, however, a large volume of shock-heated matter to scatter a sufficient number of x rays,



E15950JR

Figure 111.53

$T_e$ - $n_e$  space characterized by the electron coupling parameter  $\Gamma_{ee}$ : the ratio of the Fermi temperature  $T_F$  and the electron temperature  $T_e$ ,  $\Theta (= T_F/T_e)$ ; the average interparticle spacing  $d [= (3/4\pi n_e)^{1/3}]$ ; and Debye length  $\lambda_D$ . The plane is divided by the lines  $\Theta = 1$ ,  $\Gamma_{ee} = 1$ , and  $d = \lambda_D$  into regions where Fermi-degenerate, strongly coupled, Fermi-degenerate and strongly coupled, weakly coupled, and ideal plasmas exist. Predicted conditions of direct-drive, shock-heated experiments are shown as triangle symbols. Plasma conditions of radiatively heated targets inferred with noncollective and collective spectrally resolved x-ray scattering are shown as diamond symbols.

limiting its spatial resolution. Noncollective spectrally resolved x-ray scattering experiments reported in the literature have characterized the plasma conditions of an isochorically heated Be cylinder, a carbon foam, and a CH gas bag.<sup>13</sup> Recently, collective scattering was observed from an isochorically heated Be cylinder and was used to infer the electron density.<sup>14</sup> In principle, when collective scattering is used in conjunction with noncollective scattering, the spatially averaged quantities of electron density, electron temperature, and ionization can be diagnosed. The radiatively heated plasmas conditions are shown as the diamond symbols in Fig. 111.53.

Diagnosing plasmas that have conditions comparable to those in the shock-heated main fuel layer of a direct-drive ICF ignition target is the central focus of this article. For the first time, noncollective, spectrally resolved x-ray scattering is used to probe the plasma conditions in direct-drive, shock-heated planar plastic foils. Compared to x-ray scattering measurements from isochorically heated targets, direct-drive targets present new experimental challenges associated with the smaller physical dimensions of the target and gradients in the plasma conditions, as well as target compression and acceleration during the

scattering measurements. The scattering volumes and hence the scattered x-ray signal level of direct-drive targets are at least an order of magnitude smaller compared to the radiatively heated targets. Some direct-drive scenarios shape the adiabat in the target, which would require a spatially resolved and spectrally resolved x-ray scattering diagnostic. The direct-drive coronal plasma is in close proximity to the scattering volume and creates a major source of unwanted background x-ray continuum, which must be shielded from the detector. However, the target trajectory moves the coronal plasma into the field of view of the detector during the scattering measurement. Plastic foils are surrogates for cryogenic fuel layers. These results, required for ICF ignition, provided an opportunity to study the shell conditions of a direct-drive ICF imploded target without the cost and complexity of cryogenic hardware. The spectral line shapes of the elastic Rayleigh and the inelastic Compton components are fit to infer the electron temperature  $T_e$  and ionization  $Z$ : the Doppler-broadened Compton feature is sensitive to  $T_e$  for  $T_e$  greater than the Fermi temperature  $T_F$ , and the ratio of the Rayleigh and the Compton components is sensitive to  $Z$ .

The following sections of this article (1) describe spectrally resolved x-ray scattering; (2) present the experimental setup and simulations from the 1-D hydrodynamics code; (3) present the experimental results and compare them with the predicted plasma conditions; and (4) discuss the future use of spectrally resolved x-ray scattering to infer the plasma conditions in the main fuel layer of a direct-drive inertial confinement fusion target.

### Spectrally Resolved X-Ray Scattering

Scattering processes are classified as collective or noncollective based on the scattering parameter, defined as

$$\alpha_{\text{scatter}} = \frac{1}{k\lambda_D} = \frac{1.08 \times 10^{-4} \cdot \lambda_0(\text{cm})}{\sin(\theta/2)} \left[ \frac{n_e(\text{cm}^{-3})}{T_{\text{eff}}(\text{eV})} \right]^{1/2}, \quad (3)$$

where  $\theta$  is the scattering angle,  $k$  is the wave number of scattered x rays [ $k = 4\pi/\lambda_0 \cdot \sin(\theta/2)$ ],  $\lambda_0$  is the probe wavelength, and  $\lambda_D$  is the Debye length calculated with the effective temperature<sup>15</sup>  $T_{\text{eff}}$ , which is defined as  $T_{\text{eff}} = \sqrt{T_e^2 + T_q^2}$ , where  $T_q = T_F/(1.33 - 0.18\sqrt{r_s})$  with  $r_s = d/a_B$  ( $a_B$  is the Bohr radius).<sup>16</sup> The characteristic plasma length in the scattering parameter,  $\lambda_D$ , in Eq. (3) is replaced by the Thomas-Fermi screening length

$$\lambda_{\text{TF}} (= \sqrt{2\epsilon_0 E_F / 3n_e e^2})$$

for Fermi-degenerate plasma, and by the interparticle spacing  $d$  for strongly coupled plasma. With the use of the effective

temperature, the scattering parameter between ideal, strongly coupled, and Fermi-degenerate regimes is smoothly interpolated. For noncollective scattering ( $\alpha_{\text{scatter}} < 1$ ), x rays are scattered by individual electrons. As a result, the red wing of the Compton component in the scattered spectrum reflects the free electron velocity distribution function,<sup>17</sup> and the Doppler-broadened spectrum is sensitive to  $T_e$  for  $T_e > T_F$ . When  $T_e < T_F$ , the electron distribution becomes a Fermi distribution and its spectral shape is only weakly sensitive to the electron density. All of the scattering investigated in this article is noncollective. In the case of  $\alpha_{\text{scatter}} > 1$ , the incident x-ray photons interact with a collective electron cloud; in particular, collective scattering is of interest for electron-density measurements.<sup>14,18</sup>

Detailed calculations of the modeled x-ray scattering spectra presented here can be found in Refs. 13, 19, 20, and 21. A brief description of the model is given in this section. Spectrally resolved x-ray scattering can be modeled with the total dynamic structure factor in the differential scattering cross section. As derived by Chihara,<sup>22,23</sup> the total dynamic structure factor and the free-electron correlation function are written as

$$S(k, \omega) = |f_1(k) + q(k)|^2 S_{ii}(k, \omega) + Z_f S_{ee}^0(k, \omega) + Z_b \int \tilde{s}_{ce}(k, \omega - \omega') S_s(k, \omega') d\omega', \quad (4)$$

$$S_{ee}^0(k, \omega) = - \frac{\hbar}{1 - \exp(-\hbar \omega / k_B T_e)} \frac{\epsilon_0 k^2}{\pi e^2 n_e} \text{Im} \left[ \frac{1}{\epsilon(k, \omega)} \right]. \quad (5)$$

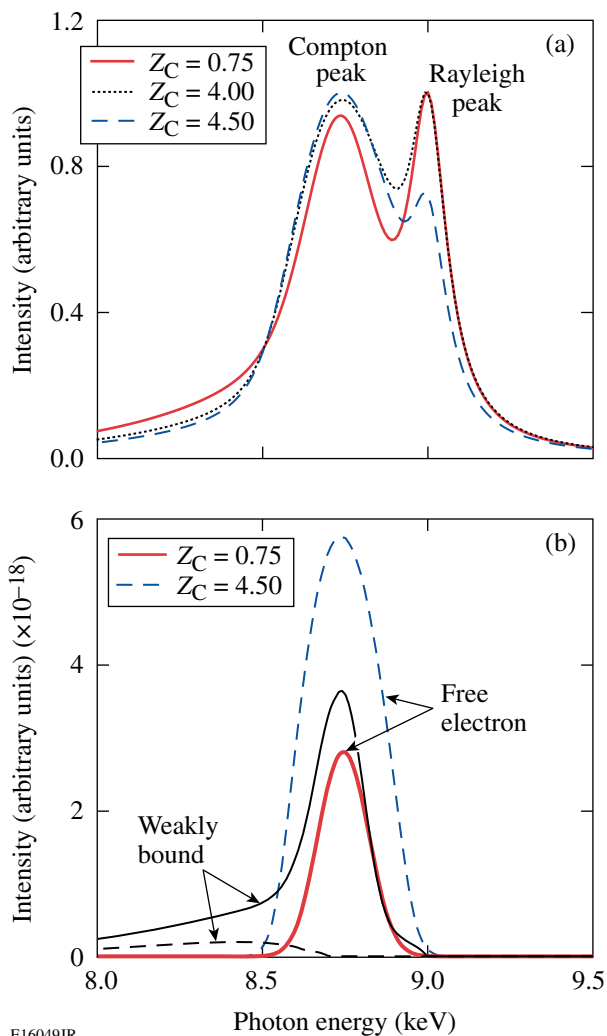
Although Eq. (4) is valid only for a single-ion component plasma, the model for the experiment under consideration includes the scattering contribution from all ion species as well as their mutual correlations as described by Gregori *et al.*<sup>13</sup> The first term on the right-hand side of Eq. (4) corresponds to the elastic Rayleigh-scattering component.  $f_1(k)$  is the ionic form factor for bound electrons and  $q(k)$  is the Fourier transform of the free-electron cloud surrounding the ion.  $S_{ii}(k, \omega)$  is the ion–ion dynamic structure factor, which describes the degree of ion–ion correlations.

In Eq. (4)  $Z_f$  and  $Z_b$  are the number of free (or valence) electrons and bound electrons, respectively. The number of electrons associated with each atom,  $Z_A$ , is the sum of  $Z_f$  and  $Z_b$ .  $Z_f$  represents electrons that are not bound to any single atom or ion including valence, delocalized, or conduction electrons. These electrons are all described in terms of plane-wave or Bloch wave functions. From a hydrodynamic perspective the useful

quantity to compare with numerical modeling is the number of free electrons or the average ionization  $Z$ , not  $Z_f$ . From the discussion above,  $Z_f$  differs from  $Z$  because it includes valence states together with kinematically free electrons. For the case of cold (undriven) plastic foil targets,  $Z_f$  is just the number of valence electrons and has no relation to  $Z$ . On the other hand, as soon as the temperature in the plastic foil is raised by the laser interaction, atomic bonds are broken and the underlying lattice responsible for the formation of the valence band is destroyed. In this case  $Z_f$  can be identified with  $Z$  and direct comparison with simulations is possible. The second term in Eq. (4) thus represents scatterings from either free or valence electrons that move independently from the ions. As shown in Eq. (5), their corresponding electron–electron correlation function  $S_{ee}^0(k, \omega)$  can be obtained through the fluctuation–dissipation theorem<sup>24</sup> in terms of the electron dielectric response function derived using the random phase approximation (RPA).<sup>25,26</sup> The RPA is accurate without any local field corrections in our noncollective scattering experiment. While the RPA is rigorously valid for kinematically free electrons, valence electrons can also be described in a similar way.<sup>27</sup> Extension to a finite band gap is also possible, but its effect is small for the conditions of this experiment.<sup>19</sup> The last term of Eq. (4) contributes to inelastic scattering from core electrons. Differently from valence and free electrons, electrons bound to localized levels in the L or K shells are treated as hydrogenic states in terms of a modified impulse approximation,<sup>28</sup> which was shown to reproduce well experimental x-ray scattering data from shock-compressed Al plasmas;<sup>29</sup> these are the bound electrons included in  $Z_b$ . This term becomes important when L-shell bound electrons are involved in the scattering process, which is the case for a carbon-hydrogen plasma, created by the laser-induced ionization of a CH ( $\text{C}_8\text{H}_8$ ) planar target. The average number of free (or valence) electrons for CH is given by

$$Z_f = \frac{Z_C + Z_H}{2} = \frac{(6 - Z_b)_C + (1 - Z_b)_H}{2}, \quad (6)$$

where  $Z_C$  and  $Z_H$  are the number of delocalized electrons in carbon and hydrogen, respectively. Figure 111.54 shows the modeled scattered spectra for CH foils using Eq. (4). Figure 111.54(a) shows the calculated total spectra including free electrons, weakly bound electrons, and tightly bound electrons. Figure 111.54(b) shows the contributions of inelastic scatterings from free electrons and weakly bound electrons to the Compton component. All spectra are calculated with an x-ray probe of 9.0-keV Zn He $_{\alpha}$ , a 130° scattering angle, and a Compton downshifted energy of 260 eV. The Compton down-



E16049JR

Figure 111.54

(a) Calculated total scattered spectra including ion, free-electron, and bound-free components for  $Z_C = 0.75$ ,  $Z_C = 4$ , and  $Z_C = 4.5$ . All spectra are normalized to the larger of either the Rayleigh or Compton peak. (b) Contributions of inelastic scatterings from free electrons and weakly bound electrons to the Compton component for  $Z_C = 0.75$  and  $Z_C = 4.5$ . The  $T_e$  and  $\rho$  are fixed to be 10 eV and 4.96 g/cm<sup>3</sup>.

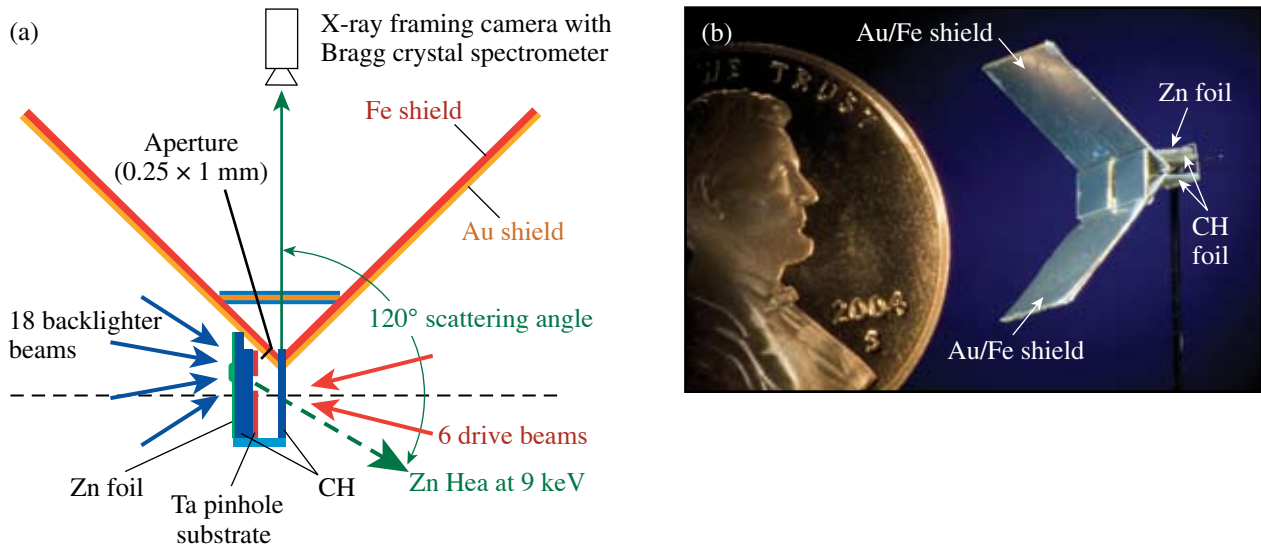
shifted energy is consistent with a 130° scattering angle, which is within the experimental tolerance of the 120° design. The calculated spectra, including all three terms in Eq. (4) for  $Z_C = 0.75$ ,  $Z_C = 4.0$ , and  $Z_C = 4.5$ , are shown in Fig. 111.54(a). In all cases discussed here  $Z_H = 1$  is set. The ratio of the Compton and Rayleigh peaks are comparable for  $Z_C = 0.75$  and  $Z_C = 4.0$ . This is because of the contribution of the scatterings from weakly bound electrons to the Compton component at low  $Z_C$ . Figure 111.54(b) shows that the contributions from the free and weakly bound electrons to the Compton component for  $Z_C =$

0.75 and  $Z_C = 4.5$ , with  $T_e = 10$  eV and  $\rho = 4.96$  g/cm<sup>3</sup>. For  $Z_C = 0.75$ , the contribution of the scattering from weakly bound electrons is slightly higher than that from the free electrons and the total intensity of the Compton peak is comparable to the Rayleigh, as shown in Fig. 111.54(a). As  $Z_C$  is increased, the Compton component is dominated by the scattering from free electrons while the ratio of the two peaks is comparable for  $Z_C = 4$ . Therefore, low ionizations of shocked CH foils (i.e.,  $Z < 2$ ) cannot be accurately diagnosed with this technique. Once a carbon K-shell electron is ionized ( $Z_C > 4$ ), the ratio of the Compton and Rayleigh peak significantly changes for CH, as shown in Fig. 111.54(a).

## Experiment

Spectrally resolved x-ray scattering experiments were performed with 90° and 120° scattering angles. The error in the exact determination of the scattering angle is estimated as  $\pm 10^\circ$ . The experimental configuration for the 120° scattering geometry is shown in Fig. 111.55(a), with a photograph of the target shown in Fig. 111.55(b). The target consists of a large Au/Fe light shield, a Zn backlighter foil, a CH drive foil, and a Ta pinhole substrate. Up to six overlapped beams smoothed with phase plates (SG8)<sup>30</sup> were used to drive a 125- $\mu$ m-thick planar CH target with a uniform intensity in an  $\sim 0.5$ -mm laser spot of  $1 \times 10^{14}$  W/cm<sup>2</sup>. Eighteen additional tightly focused beams ( $\sim 100$ - $\mu$ m spot) irradiated the Zn foil with an overlapped intensity of  $\sim 10^{16}$  W/cm<sup>2</sup> and generated a point-source backlighter of Zn He $_{\alpha}$  emission at 9.0 keV. The 0.5-mm-thick CH foil positioned between the Zn foil and the Ta pinhole substrate blocked x rays with photon energies less than  $\sim 4$  keV with minimal attenuation to the Zn K-shell emission. This prevented the Zn backlighter from radiatively heating the target. The Ta pinhole substrate with a 400- $\mu$ m-diam aperture restricted the backlighter illumination of the CH drive foil to the portion of the target that was uniformly shock heated. The scattering angle was reduced to 90° by adjusting the locations of the aperture and the focal position of the backlighter beams.

Most of the Zn He $_{\alpha}$  emission propagates through the drive foil; however, a small fraction of the x rays are scattered. X rays scattered at 90° or 120° were dispersed with a Bragg crystal spectrometer and recorded with an x-ray framing camera<sup>31</sup> outfitted with a charge-coupled-device (CCD) camera. A highly oriented pyrolytic graphite (HOPG)<sup>32</sup> crystal with a 2d spacing of 6.7 Å was used in the mosaic focusing mode<sup>33</sup> to provide high reflectivity of the scattered x-ray spectrum.<sup>34</sup> The Au/Fe shields reduced the measured background x-ray continuum levels by blocking the direct lines of sight to the Zn and CH coronal plasmas.

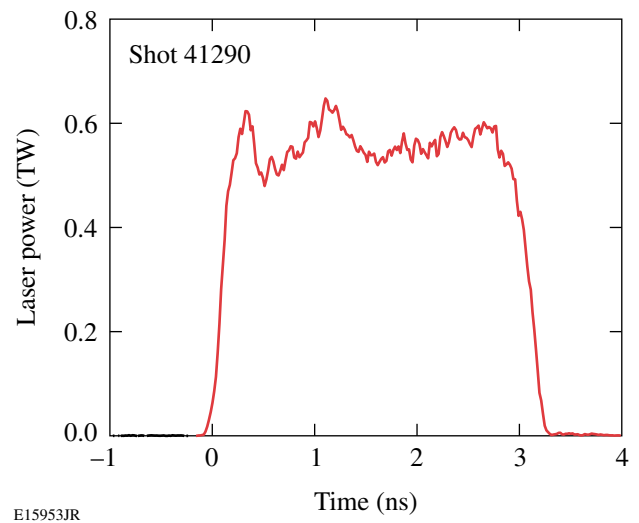


E15952JR

Figure 111.55

(a) Target design of the noncollective spectrally resolved x-ray scattering experiment on OMEGA using a  $120^\circ$  scattering geometry; (b) a photograph of an x-ray scattering target compared in size to a penny.

The strategy of the experiment was to drive a shock wave through the CH foil and to scatter the  $\text{Zn He}_\alpha$  x rays from the uniformly compressed portion of the shock-heated CH around the time that the shock breaks out of the rear side of the target (i.e., the side opposite the laser-irradiated side). Two drive conditions were examined: undriven (i.e., cold, uncompressed CH foil) and an  $\alpha = 3$  drive. The measured time history of the laser power for the  $\alpha = 3$  drive is presented in Fig. 111.56. The plasma conditions of directly driven CH foils were simulated with the 1-D hydrodynamics code *LILAC*. A detailed description of *LILAC* can be found elsewhere<sup>35</sup> with the main features of the code described in this section. Laser absorption is calculated using a ray-trace algorithm that models inverse bremsstrahlung. Transport of radiation is modeled through multigroup diffusion with the Los Alamos National Laboratory Astrophysical Tables<sup>36</sup> or an average ion model providing the opacities. The *SESAME* tables are used to model the equation of state. *LILAC* uses a flux-limited<sup>37</sup> Spitzer–Härm<sup>38</sup> electron thermal-conduction model. This drive is predicted to create a 15-Mbar shock-wave pressure. Figure 111.57 shows the spatial profile of the predicted plasma conditions created with an  $\alpha = 3$  drive around the time the shock breaks out the rear side of the target. A single shock is launched by the  $\alpha = 3$  drive and breaks out the rear side of the target at 2.7 ns. The measurement was made around the shock-breakout time. The plasma conditions in the CH at the time of shock breakout are predicted to be fairly uniform. For the  $\alpha = 3$  drive, the foil is predicted to be heated to  $T_e = 12$  eV with an average ionization

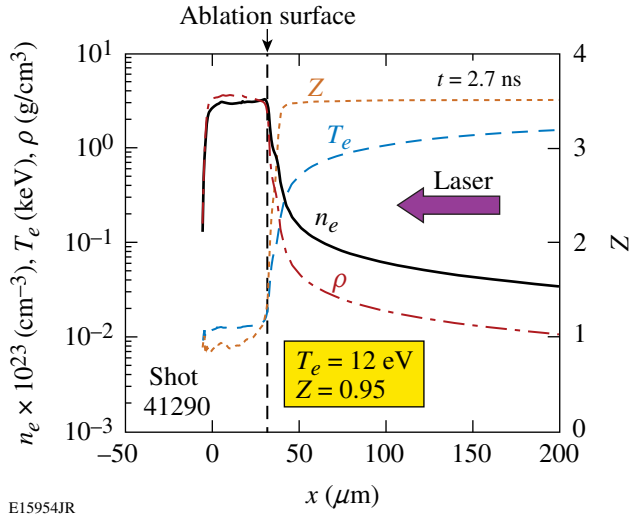


E15953JR

Figure 111.56

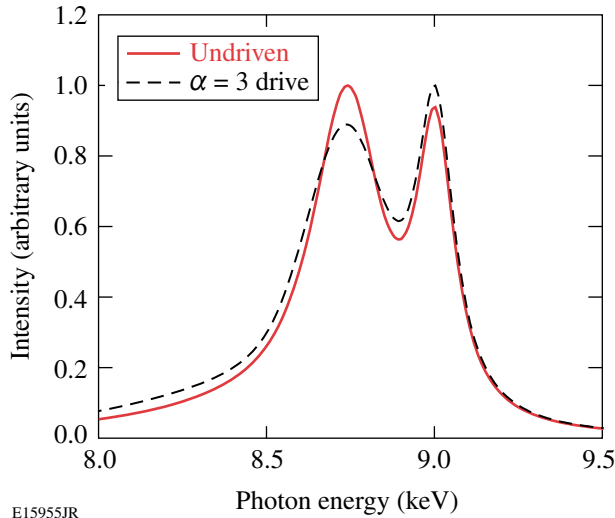
The measured laser pulse for the  $\alpha = 3$  drive (shot 41290).

$Z = 0.95$ . As shown in Fig. 111.58, there is little difference in the predicted x-ray scattered spectra from the CH foil targets for undriven and  $\alpha = 3$  drive cases. The plasma condition for an undriven case is  $T_e = 0.1$  eV and  $Z_C = 0.1$ . The ion temperature is predicted to be equal to the electron temperature for all of the drive cases under consideration. The spatially integrated, time-resolved spectra were collected over a 500-ps integration time, which is short compared to the hydrodynamic time scales of the experiment.



E15954JR

Figure 111.57  
Predictions from the 1-D hydrodynamics code *LILAC* of the spatial profiles of electron temperature ( $T_e$ ), electron density ( $n_e$ ), average ionization ( $Z$ ), and mass density ( $\rho$ ) for laser-irradiated CH foil targets with  $\alpha = 3$  drive.



E15955JR

Figure 111.58  
Predicted x-ray scattered spectra for undriven and  $\alpha = 3$  driven CH foils.

The total number of the detected photons per nanosecond,  $N_{\text{det}}$ , was estimated for the x-ray scattering experiment. It is given by

$$N_{\text{det}} = \left( \frac{E_L}{h\nu} \eta_L \frac{1}{\tau_L} \right) \left( \frac{\Omega_{\text{pinhole}}}{4\pi} \right) \eta_{\text{CH}} \times \left[ \frac{n_e \sigma_{T^x}}{(1 + \alpha_{\text{scatter}})^2} \right] \left( \frac{\Omega_{\text{detector}}}{4\pi} R_{\text{crystal}} \eta_d \right), \quad (7)$$

where  $E_L$  is the laser energy,  $\tau_L$  is the laser pulse duration,  $\eta_L$  is the conversion efficiency from the laser energy into the 9.0-keV x rays,  $\eta_{\text{CH}}$  is the attenuation due to 500  $\mu\text{m}$  of CH,  $n_e$  is the electron density,  $x$  is the thickness of the compressed target,  $\Omega_{\text{pinhole}}$  and  $\Omega_{\text{detector}}$  are the solid angles limited by the pinhole diameter and crystal size,  $R_{\text{crystal}}$  is the integrated reflectivity of the crystal, and  $\eta_{\text{CH}}$  is the efficiency inside the detector, including the MCP efficiency and filter transmission. Using  $E_L = 280 \text{ J} \times 18$  beams in the 3-ns pulse,  $h\nu = 9.0 \text{ keV}$ ,  $\eta_L$  is assumed to be  $\sim 0.1\%$ ,  $\Omega_{\text{pinhole}}/4\pi = 0.04$ ,  $\eta_{\text{CH}} = 85\%$ ,  $n_e = 1.5 \times 10^{23} \text{ cm}^{-3}$ ,  $x = 40 \mu\text{m}$  for a shock-compressed target with the  $\alpha = 3$  drive,  $\alpha_{\text{scatter}} = 0.2$  for the  $120^\circ$  scattering geometry,  $\Omega_{\text{detector}}/4\pi = 5.7 \times 10^{-3}$ ,  $R_{\text{crystal}} = 2 \times 10^{-3}$ , and  $\eta_d = 1\%$ . Using Eq. (7),  $N_{\text{det}}$  is estimated to be  $\sim 1500$  photons/ns. Since the integration time was 500 ps and the spectrum was dispersed over the  $\sim 90$  spectrally resolved bins ( $\sim 10 \text{ eV/bin}$ ), the estimated ratio of the signal due to photon statistics is 8.2, which is consistent with the measured signal-to-noise ratio of 8.

## Results and Discussion

X-ray spectra detected at  $90^\circ$  and  $120^\circ$  scattering angles were recorded for an undriven CH foil. Figure 111.59(a) shows the measured spectra from undriven CH foils in  $90^\circ$  and  $120^\circ$  scattering geometries, as well as the signal from a control target whose drive foil has a 1-mm-diam thru-hole in the center of the foil. Figure 111.59(b) shows a microscope image of the control target. The purpose of the control shot was to experimentally confirm that the measured x rays were scattered from the intended target. The lack of signal measured for this shot indicates that x rays are scattering from the intended portion of the nominal drive foil (i.e., without a thru-hole), and scattering from other unintended sources is negligible. The Compton peaks of measured spectra with  $90^\circ$  and  $120^\circ$  scattering angles are consistent with the calculated Compton downshifted energies of  $E_C = \hbar^2 k^2 / 2m_e = 158 \text{ eV}$  and  $238 \text{ eV}$ , respectively. In this article, all of the x-ray scattering measurements from the driven foils were taken with the  $120^\circ$  scattering angle; however, measurements from two different scattering angles would be beneficial to determine the accuracy of the experimentally determined values of  $T_e$  and  $Z_f$ .

The spectra of x rays detected at a  $120^\circ$  scattering angle are presented in Fig. 111.60(a) for the CH targets and in Fig. 111.60(b) for the Br-doped CH targets for the two drive conditions under consideration (i.e., undriven and  $\alpha = 3$  drive). The Br-dopant concentration level in the CH foil was 2% atomic in the bulk of the target, but no Br was in the ablator portion of the target. All of the spectra in Fig. 111.60 are normalized to the larger peak of the Rayleigh or Compton feature. The location

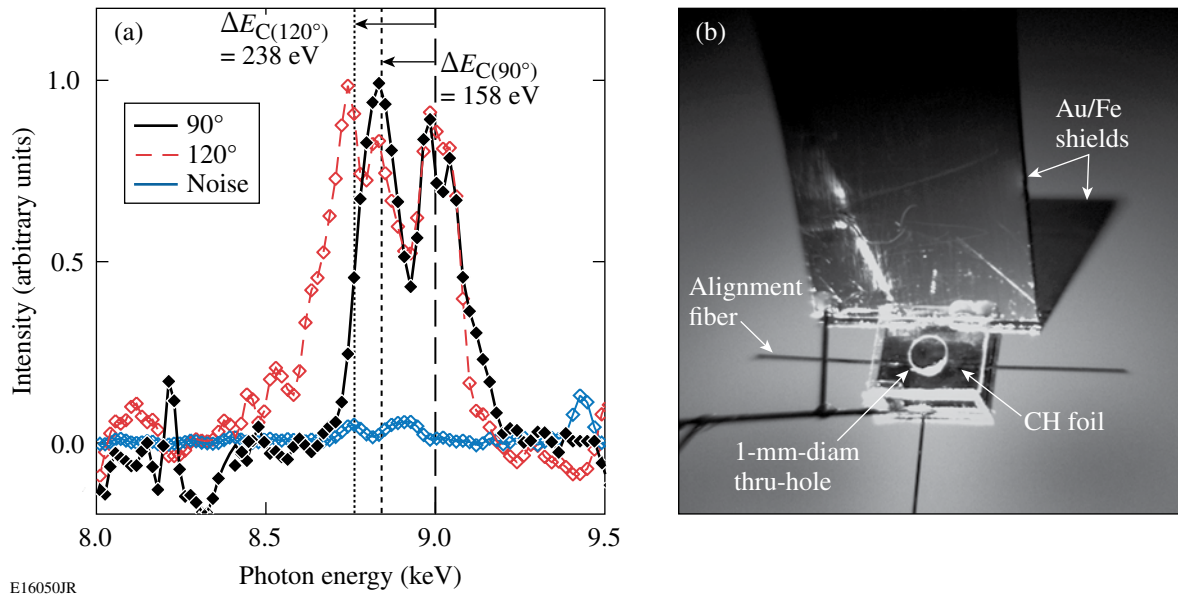


Figure 111.59

(a) Measured x-ray spectra scattered from undriven CH targets with  $90^\circ$  and  $120^\circ$  scattering geometries are compared with the noise level. The dotted and dashed vertical lines show the Compton downshifted energy of 158 eV/238 eV for the  $90^\circ/120^\circ$  scattering angles. (b) A microscope image of the control target with a 1-mm-diam thru-hole in the center of the CH foil.

of line emissions of  $\text{Zn He}_\alpha$  at 9.0 keV and  $\text{Zn Ly}_\alpha$  at 9.3 keV is indicated with vertical dotted lines in the figure. A comparison of the spectra scattered from the CH targets shows little difference between the driven and undriven targets. A detailed analysis of the measured spectra with models is presented in Figs. 111.61(a) and 111.61(b). A similar comparison for the x-ray spectra from the Br-doped CH shows significant changes in the heights of the Compton feature.  $\text{Zn Ly}_\alpha$  line emission contributes to the blue wings of the measured Rayleigh features. For the quantitative analysis, the measured spectra were fit with models to infer  $T_e$  and  $Z_b$  for each ion in the plasma as described in Eq. (6). The modeled spectra were calculated as described in **Spectrally Resolved X-Ray Scattering** (p. 192), and a best fit to the measured spectra was obtained using a least-squares-fitting routine that varied  $T_e$  and the  $Z_b$ 's.

The experimental scattered spectrum from the cold, undriven target is compared with three modeled spectra in Fig. 111.61(a). All of the modeled spectra have solid densities ( $\rho = 1.24 \text{ g/cm}^3$ ) and low electron temperatures ( $T_e = 0.1 \text{ eV}$ ) to indicate that no ionization in CH has occurred, but the  $Z_C$  is varied from 0.1 to 4. The lowest  $Z_C$  agrees with the experimental result as expected in cold CH; however, the models are not very sensitive to  $Z_C$  for  $Z_C < 2$ , suggesting that valence electrons in cold CH could scatter x rays like free electrons. In order to investigate the  $T_e$  sensitivity in the case of driven CH,

$Z_f$  was set to 2.5 (corresponding to  $Z_C = 4$  and  $Z_H = 1$  delocalized electrons) shown in Fig. 111.61(b). As mentioned before, in this case all of the carbon bonds are destroyed and  $Z_f$  does indeed represent the average ionization state in the plasma. In addition to scattering from valence electrons, scattering from the remaining bound electrons into L and K shells must be included, with the respective ionization levels corrected for continuum lowering.<sup>39</sup> In Fig. 111.61(b), the measured spectrum of the CH foil for the  $\alpha = 3$  drive is compared with the modeled spectra for three electron temperatures:  $T_e = 1, 10,$  and  $20 \text{ eV}$  with  $Z_C = 4$ . The mass density used in the models is four times solid density ( $\rho = 4.96 \text{ g/cm}^3$ ), as suggested by *LILAC* simulations. Since the measured spectrum from the driven CH is bounded by the models with  $T_e = 1 \text{ eV}$  and  $T_e = 20 \text{ eV}$ , an upper limit of  $T_e = 20 \text{ eV}$  is inferred for the  $\alpha = 3$  drive. As described in Fig. 111.54(b), the ratios of the Compton and Rayleigh peaks are comparable when  $Z_C < 4$  in a driven CH. Therefore, the inferred  $Z$  in this experiment is an upper limit of  $Z \sim 2$ . The predicted spectra show that the width of the Compton peak is not very sensitive to the electron temperature because  $T_e$  is comparable to the Fermi temperature  $T_F = 16 \text{ eV}$  from the hydro calculation ( $n_e \sim 3 \times 10^{23} \text{ cm}^{-3}$  and  $Z \sim 1$ ). It is also noted that for the compressed case with  $\alpha = 3$ , the electron density is  $n_e \sim 3 \times 10^{23} \text{ cm}^{-3}$ , which lowers the continuum by  $\sim 20 \text{ eV}$  (Ref. 20); thus a fraction of the L-shell electrons should be indeed delocalized.

Trace amounts of Br in the CH foil (i.e., 2% atomic concentration) increase the sensitivity of the spectrally resolved x-ray spectra to changes in the electron temperature. The experimental spectra scattered from CHBr targets are presented in Fig. 111.62 for the two drives under consideration, along with the fitted spectra. A comparison of the scattered x-ray spectra from

the undriven CHBr target [see Fig. 111.62(a)] with the undriven CH target [see Fig. 111.61(a)] reveals that the Br dopant enhances the ratio of the Rayleigh peak to the Compton peak. This is a consequence of the increased number of tightly bound electrons in the CHBr foil. The models for scattered spectra of CHBr foils include the scattering contributions from all ionic species as

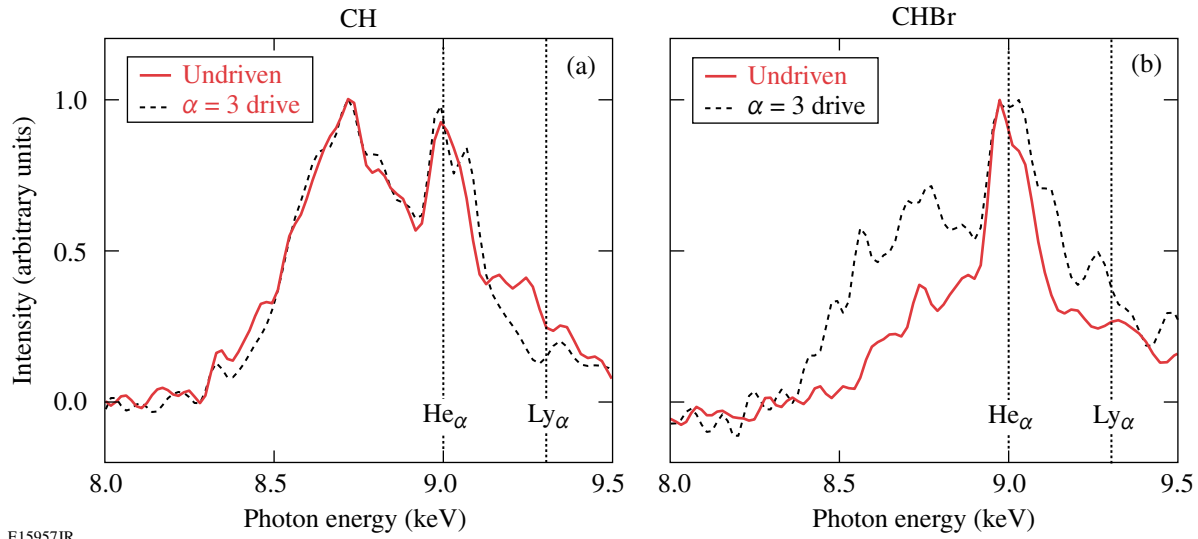


Figure 111.60

(a) Measured x-ray spectra scattered from (a) CH and (b) CHBr targets with the following drive conditions: undriven and  $\alpha = 3$  drive. Spectra are normalized at the Rayleigh peak. The spectral location of Zn  $He_\alpha$  at 9.0 keV and Zn  $Ly_\alpha$  at 9.3 keV is indicated with vertical dotted lines.

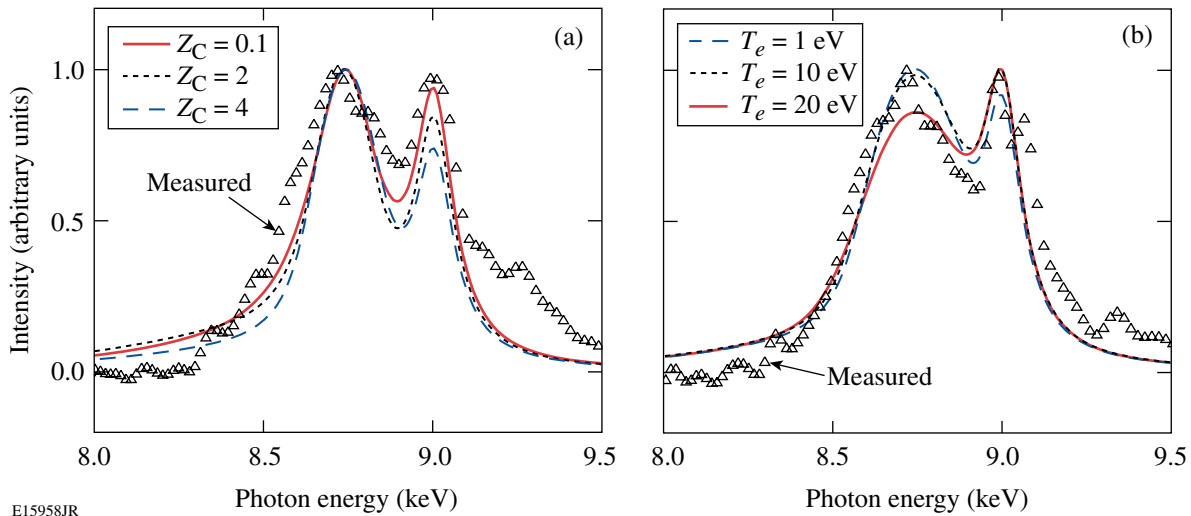
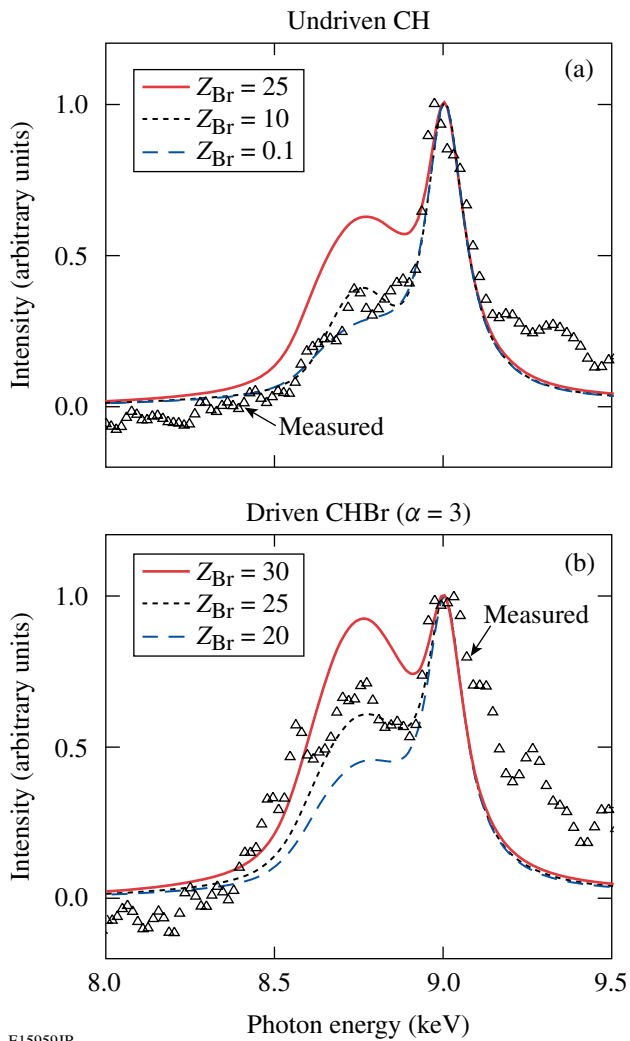


Figure 111.61

(a) Measured spectrum from the undriven CH target compared with modeled spectra for  $Z_C = 0.1$ ,  $Z_C = 2$ , and  $Z_C = 4$  with  $T_e = 0.1$  eV. (b) Measured spectrum for the  $\alpha = 3$  drive compared with modeled spectra of  $T_e = 1$ , 10, and 20 eV, and  $Z_C = 4$ .



E15959JR

Figure 111.62

Measured x-ray spectra scattered from CHBr targets for (a) undriven and (b)  $\alpha = 3$  drive are compared with modeled spectra varying  $Z_{\text{Br}}$ . The inferred parameters are  $T_e = 0.1$  eV and  $Z_f = 2.6$  for undriven and  $T_e = 10$  eV and  $Z_f = 2.9$  for the  $\alpha = 3$  drive.  $Z_C = 4$  was set for both undriven and driven cases.

well as their mutual correlations. In addition, the attenuation of the scattered x rays due to the path length in the CHBr foil is included in the modeled scattered spectra. The electron temperatures inferred from the spectral fitting for the undriven and  $\alpha = 3$  drive are  $T_e = 0.1$  eV and  $T_e = 10$  eV, respectively, which are similar to the observations for the pure CH foils. Adding the Br dopant increases the sensitivity of the x-ray scattering to changes in  $Z$ . As shown in Fig. 111.60(b), the height of the Compton feature is increased for the driven target, in contrast to the results with the CH target shown in Fig. 111.60(a). The density is assumed to be solid density for undriven and four

times solid density for  $\alpha = 3$  drive. The undriven case has  $Z_{\text{Br}} = 10$ ,  $Z_C = 4$ , and  $Z_H = 1$ ; the  $\alpha = 3$  drive has  $Z_{\text{Br}} = 25$ ,  $Z_C = 4$ , and  $Z_H = 1$ . The ratio of the Rayleigh peak to the Compton peak is primarily dependent on  $Z_{\text{Br}}$ . It is observed that  $Z_{\text{Br}}$  increases for the driven CHBr foil, while  $Z_C$  is not very sensitive to the  $\alpha = 3$  drive. For the undriven case, little differences are seen between  $Z_{\text{Br}} = 0.1$  and  $Z_{\text{Br}} = 10$ , while  $Z_{\text{Br}}$  needs to be increased close to  $Z_{\text{Br}} = 25$  to match the model to data for the driven case. Since the binding energy of 257 eV for a 3-s M-shell electron of a neutral bromine atom is comparable to the Compton downshifted energy of  $\sim 240$  eV, electrons of a bromine ion in the M and N shell (25 electrons) can be ionized with the Zn He $_{\alpha}$  x rays. Due to the high electron densities in the compressed plasma, continuum lowering is likely to be responsible for the large number of delocalized electrons in bromine. Those electrons belong to extended M and N shells for which electron bonding to the ion core may be heavily screened in the dense plasma. The values of  $Z_f$  inferred from the spectral fitting are  $Z_f = 2.6$  and  $Z_f = 2.9$  for the undriven and  $\alpha = 3$  drive, respectively.

The electron temperatures predicted with *LILAC* for the shocked CH and CHBr targets ( $T_e = 12$  eV) are comparable with the measured results ( $T_e = 10$  to 20 eV) for a drive intensity of  $1 \times 10^{14}$  W/cm $^2$ ; however, an experimental accuracy for  $T_e$  of 10% to 20% is needed to validate the simulations from the hydrodynamics codes. Attempts were made to increase the electron temperature in the direct-drive target by increasing the laser drive intensity to  $\sim 10^{15}$  W/cm $^2$ . However, the x-ray background levels measured for higher drive intensities were found to overwhelm the scattered x-ray spectrum.

### Future Application

The main objective of this research is to develop techniques to probe the plasma conditions in the DT shell of a direct-drive implosion target during the laser irradiation to diagnose the shell adiabat. X-ray scattering is an attractive option for this application since it is noninvasive. The experimental results presented here demonstrate that it is possible to infer the spatially averaged electron temperature of a nearly Fermi-degenerate, direct-drive, shock-heated, and compressed CH foil. The complications arising from the L-shell electrons of carbon associated to a structural phase transition from the solid state to plasma will not be present in the fully ionized hydrogen isotope plasma comprising the shell of the ICF target. Consequently, a straightforward interpretation of the spatially averaged quantities of electron temperature and average ionization in the shell of a DT ICF implosion target is expected from the noncollective x-ray scattering. Predicted x-ray-scattering spectra from

an imploding cryogenic capsule in hohlraum are discussed in Ref. 40. The recent observations of plasmons in warm dense matter<sup>14</sup> show that it is possible to infer the electron density from the collective, forward x-ray scattering. Therefore, a combination of collective and noncollective x-ray scattering should provide the capability to diagnose the spatially averaged quantities of electron density, electron temperature, and the average ionization of a direct-drive DT cryogenic implosion target.

## Conclusion

The electron temperature ( $T_e$ ) and average ionization ( $Z$ ) of nearly Fermi-degenerate, direct-drive, shock-heated, and compressed CH planar foils were investigated for the first time using noncollective spectrally resolved x-ray scattering on the OMEGA Laser System. CH and Br-doped CH foils were driven with six beams, having an overlapped intensity of  $1 \times 10^{14}$  W/cm<sup>2</sup> and generating 15-Mbar pressure in the foil. An examination of the scattered x-ray spectra reveals an upper limit of  $Z \sim 2$ , and  $T_e = 20$  eV is inferred from the spectral line shapes of the elastic Rayleigh and inelastic Compton components. The electron temperatures predicted with *LILAC* ( $T_e = 12$  eV) were found to be comparable with the measured results ( $T_e = 10$  to 20 eV). Low average ionizations (i.e.,  $Z < 2$ ) cannot be accurately diagnosed in this experiment due to the difficulties in distinguishing delocalized valence or free electrons. Trace amounts of Br in the CH foil (i.e., 2% atomic concentration) were shown to increase the sensitivity of the noncollective, spectrally resolved x-ray scattering to changes in the average ionization. A combination of noncollective and collective spectrally resolved x-ray scattering looks like a promising diagnostic technique to probe the spatially averaged plasma conditions in the DT shell of a direct-drive implosion target during the laser irradiation to diagnose the shell adiabat.

## ACKNOWLEDGMENT

The authors are grateful to the LLE Target Fabrication Group, especially Mark Bonino and Dave Turner, for their expertise in constructing the spectrally resolved x-ray scattering targets, as well as Laser Facility Manager Keith Thorp and the OMEGA operations crew for providing the highly reproducible laser performance. This work was supported by the U.S. Department of Energy Office of Inertial Confinement Fusion under Cooperative Agreement No. DE-FC52-92SF19460, the University of Rochester, and the New York State Energy Research and Development Authority. The support of DOE does not constitute an endorsement by DOE of the views expressed in this article.

## REFERENCES

1. J. Nuckolls *et al.*, *Nature* **239**, 139 (1972); J. D. Lindl, R. L. McCrory, and E. M. Campbell, *Phys. Today* **45**, 32 (1992); R. L. McCrory, J. M. Soures, C. P. Verdon, F. J. Marshall, S. A. Letzring, S. Skupsky, T. J. Kessler, R. L. Kremens, J. P. Knauer, H. Kim, J. Delettrez, R. L. Keck, and D. K. Bradley, *Nature* **335**, 225 (1988); R. L. McCrory, S. P. Regan, S. J. Loucks, D. D. Meyerhofer, S. Skupsky, R. Betti, T. R. Boehly, R. S. Craxton, T. J. B. Collins, J. A. Delettrez, D. Edgell, R. Epstein, K. A. Fletcher, C. Freeman, J. A. Frenje, V. Yu. Glebov, V. N. Goncharov, D. R. Harding, I. V. Igumenshchev, R. L. Keck, J. D. Kilkenny, J. P. Knauer, C. K. Li, J. Marciante, J. A. Marozas, F. J. Marshall, A. V. Maximov, P. W. McKenty, J. Myatt, S. Padalino, R. D. Petrasso, P. B. Radha, T. C. Sangster, F. H. Séguin, W. Seka, V. A. Smalyuk, J. M. Soures, C. Stoeckl, B. Yaakobi, and J. D. Zuegel, *Nucl. Fusion* **45**, S283 (2005).
2. P. W. McKenty, V. N. Goncharov, R. P. J. Town, S. Skupsky, R. Betti, and R. L. McCrory, *Phys. Plasmas* **8**, 2315 (2001).
3. P. W. McKenty, T. C. Sangster, M. Alexander, R. Betti, R. S. Craxton, J. A. Delettrez, L. Elasky, R. Epstein, A. Frank, V. Yu. Glebov, V. N. Goncharov, D. R. Harding, S. Jin, J. P. Knauer, R. L. Keck, S. J. Loucks, L. D. Lund, R. L. McCrory, F. J. Marshall, D. D. Meyerhofer, S. P. Regan, P. B. Radha, S. Roberts, W. Seka, S. Skupsky, V. A. Smalyuk, J. M. Soures, K. A. Thorp, M. Wozniak, J. A. Frenje, C. K. Li, R. D. Petrasso, F. H. Séguin, K. A. Fletcher, S. Padalino, C. Freeman, N. Izumi, J. A. Koch, R. A. Lerche, M. J. Moran, T. W. Phillips, G. J. Schmid, and C. Sorce, *Phys. Plasmas* **11**, 2790 (2004).
4. M. C. Herrmann, M. Tabak, and J. D. Lindl, *Phys. Plasmas* **8**, 2296 (2001).
5. R. Betti, K. Anderson, V. N. Goncharov, R. L. McCrory, D. D. Meyerhofer, S. Skupsky, and R. P. J. Town, *Phys. Plasmas* **9**, 2277 (2002).
6. S. P. Regan, J. A. Delettrez, V. N. Goncharov, F. J. Marshall, J. M. Soures, V. A. Smalyuk, P. B. Radha, B. Yaakobi, R. Epstein, V. Yu. Glebov, P. A. Jaanimagi, D. D. Meyerhofer, T. C. Sangster, W. Seka, S. Skupsky, C. Stoeckl, D. A. Haynes, Jr., J. A. Frenje, C. K. Li, R. D. Petrasso, and F. H. Séguin, *Phys. Rev. Lett.* **92**, 185002 (2004).
7. National Research Council (U.S.) Committee on High Energy Density Plasma Physics, *Frontiers in High Energy Density Physics: The X-Games of Contemporary Science* (National Academies Press, Washington, DC, 2003).
8. S. Ichimaru, *Rev. Mod. Phys.* **54**, 1017 (1982).
9. S. H. Glenzer *et al.*, *Phys. Plasmas* **6**, 2117 (1999).
10. S. H. Glenzer *et al.*, *Phys. Rev. Lett.* **90**, 175002 (2003); O. L. Landen *et al.*, *J. Quant. Spectrosc. Radiat. Transf.* **71**, 465 (2001).
11. T. R. Boehly, J. A. Delettrez, J. P. Knauer, D. D. Meyerhofer, B. Yaakobi, R. P. J. Town, and D. Hoarty, *Phys. Rev. Lett.* **87**, 145003 (2001); D. J. Hoarty *et al.*, *J. Quant. Spectrosc. Radiat. Transf.* **99**, 283 (2006).
12. H. Sawada, S. P. Regan, R. Epstein, D. Li, V. Goncharov, P. B. Radha, D. D. Meyerhofer, T. R. Boehly, V. A. Smalyuk, T. C. Sangster, B. Yaakobi, and R. C. Mancini, "Investigation of Direct-Drive Shock-Heating Using X-Ray Absorption Spectroscopy," to be submitted to *Physics of Plasmas*.
13. G. Gregori, S. H. Glenzer, H. K. Chung, D. H. Froula, R. W. Lee, N. B. Meezan, J. D. Moody, C. Niemann, O. L. Landen, B. Holst, R. Redmer, S. P. Regan, and H. Sawada, *J. Quant. Spectrosc. Radiat. Transf.* **99**, 225 (2006).

14. S. H. Glenzer *et al.*, Phys. Rev. Lett. **98**, 065002 (2007).
15. M. W. C. Dharma-wardana and F. Perrot, Phys. Rev. Lett. **84**, 959 (2000).
16. F. Perrot and M. W. C. Dharma-wardana, Phys. Rev. B **62**, 16,536 (2000).
17. J. Sheffield, *Plasma Scattering of Electromagnetic Radiation* (Academic Press, New York, 1975).
18. M. K. Urry *et al.*, J. Quant. Spectrosc. Radiat. Transf. **99**, 636 (2006).
19. G. Gregori, S. H. Glenzer, and O. L. Landen, Phys. Rev. E **74**, 026402 (2006).
20. G. Gregori *et al.*, Phys. Plasmas **11**, 2754 (2004).
21. G. Gregori, S. H. Glenzer, and O. L. Landen, J. Phys. A, Math. Gen. **36**, 5971 (2003).
22. J. Chihara, J. Phys. F, Met. Phys. **17**, 295 (1987).
23. J. Chihara, J. Phys., Condens. Matter **12**, 231 (2000).
24. R. Kubo, J. Phys. Soc. Jpn. **12**, 570 (1957).
25. D. Pines and D. Bohm, Phys. Rev. **85**, 338 (1952).
26. D. Pines and P. Nozieres, *Theory of Quantum Liquids*, Advanced Book Classics (Addison-Wesley, Reading, MA, 1989).
27. P. Nozières and D. Pines, Phys. Rev. **113**, 1254 (1959).
28. M. Schumacher, F. Smend, and I. Borchert, J. Phys. B, At. Mol. Phys. **8**, 1428 (1975).
29. D. Riley *et al.*, Laser Part. Beams **25**, 1 (2007).
30. S. P. Regan, J. A. Marozas, J. H. Kelly, T. R. Boehly, W. R. Donaldson, P. A. Jaanimagi, R. L. Keck, T. J. Kessler, D. D. Meyerhofer, W. Seka, S. Skupsky, and V. A. Smalyuk, J. Opt. Soc. Am. B **17**, 1483 (2000).
31. C. J. Pawley and A. V. Deniz, Rev. Sci. Instrum. **71**, 1286 (2000); R. E. Turner *et al.*, Rev. Sci. Instrum. **72**, 706 (2001).
32. A. Pak *et al.*, Rev. Sci. Instrum. **75**, 3747 (2004).
33. B. Yaakobi and A. J. Burek, IEEE J. Quantum Electron. **QE-19**, 1841 (1983).
34. F. J. Marshall and J. A. Oertel, Rev. Sci. Instrum. **68**, 735 (1997).
35. J. Delettrez, R. Epstein, M. C. Richardson, P. A. Jaanimagi, and B. L. Henke, Phys. Rev. A **36**, 3926 (1987); J. Delettrez, Can. J. Phys. **64**, 932 (1986).
36. W. F. Huebner *et al.*, Los Alamos National Laboratory, Los Alamos, NM, Report LA-6760-M (1977).
37. R. C. Malone, R. L. McCrory, and R. L. Morse, Phys. Rev. Lett. **34**, 721 (1975).
38. L. Spitzer, Jr. and R. Härm, Phys. Rev. **89**, 977 (1953).
39. J. A. Bearden and A. F. Burr, Rev. Mod. Phys. **39**, 125 (1967).
40. A. L. Kritcher *et al.*, High Energy Density Phys. **3**, 156 (2007).

